Archives of Hydro-Engineering and Environmental Mechanics
Vol. 55 (2008), No. 3–4, pp. 95–124

Size Effects in Problems of Footings on Sand within Micro-Polar Hypoplasticity

Jacek Tejchman, Jarosław Górski

Faculty of Civil and Environmental Engineering, Gdańsk University of Technology
Narutowicza 11/12, 80-952 Gdansk, Poland
e-mails: tejchmk@pg.gda.pl, jgorski@pg.gda.pl

(Received September 28, 2008; revised March 25, 2009)

Abstract

Numerical FE investigations of size effects in problems of footings on sand were performed. Micro-polar hypoplastic constitutive model was used to describe a mechanical behaviour of a cohesionless granular material during a monotonic deformation path. The FE analyses were carried out with three different footing widths. In deterministic calculations, a uniform distribution of initial void ratio was used. In statistical calculations, initial void ratios took the form of random spatial fields described by a truncated Gaussian random distribution. In order to reduce the number of stochastic realizations without sacrificing the accuracy of the calculations, a stratified sampling method was applied. The numerical results were compared with corresponding laboratory tests by Tatsuoka et al (1997). The numerical results show that the bearing capacity of footings decreases with increasing specimen size. If the initial void ratio is stochastically distributed, the mean bearing capacity of footings may be larger than the deterministic value. The statistical size effect is smaller than the deterministic one.

Key words: footing, micro-polar hypoplasticity, sand, shear localization, size effects, stratified sampling, void ratio

1. Introduction

The size effect phenomenon (experimental results vary with the size of specimens) is an inherent property of the behaviour of many engineering materials. In the case of cohesionless granular bodies, shear resistance increases with decreasing specimen size and increasing mean grain diameter during many experiments including shear localization (Wernick 1978, Tatsuoka et al 1997, Tejchman 2004a). Thus, results from laboratory tests which are scaled versions of the actual structures cannot be directly transferred to them. Much as in quasi-brittle materials (Bazant and Planas 1998), two main size effects can be distinguished: deterministic and statistical. The first is caused by strain localization which cannot be appropriately scaled in laboratory tests. The specimen strength increases with increasing ratio l_c/L (l_c – characteristic length of microstructure influencing both the thickness and

spacing of shear localization, L – specimen size). In addition, this feature is strongly influenced by pressure level (Tatsuoka et al 1997) since friction ratio and dilatancy decrease with increasing pressure. A statistical (or stochastic) effect is caused by the spatial randomness of material properties. According to Weibull's theory (Weibull 1951), this effect is caused by weak spots whose relative amount usually grows with increasing specimen size. Thus, the strength diminishes with increasing specimen size. Up to now, such size effects have not been taken into account in specifications such as design codes for engineering structures. The physical understanding of size effects is of major importance for civil engineers who are forced to extrapolate experimental outcomes at laboratory scale (large geosystems or structures are usually beyond the range of testing in laboratories) to results which can be used in real scale situations.

In the case of granular materials involving shear localization, empirical size effect laws are not known (in contrast to geometrically similar brittle specimens) (Bazant and Planas 1998) as the performance of laboratory tests with large specimens is more complex than in the case of brittle solids. In addition, the effect of pressure cannot be neglected.

The intention of the numerical simulations for this paper is to investigate a deterministic and statistical size effect in problems of footings on cohesionless granular material like sand under quasi-static conditions by considering the influence of shear localization on shear resistance. A finite element method with a micro-polar hypoplastic constitutive model (Tejchman and Gudehus 2001, Tejchman and Niemunis 2006, Tejchman and Górski 2008) was used, which is able to describe the essential properties of granular bodies during shear localization in a wide range of pressures and densities during monotonic deformation paths. The calculations were performed with three different footing widths. Deterministic calculations were performed with a uniform distribution of the initial void ratio in dense sand. Statistical analyses were carried out with spatially correlated homogeneous distributions of the initial void ratio in dense sand, which were assumed to be random. Truncated Gaussian random fields were generated using a conditional rejection method (Walukiewicz et al 1997) for weakly correlated random fields. The approximated results were obtained using a stratified sampling method belonging to a group of reduced Monte Carlo methods (Hurtado and Barbat 1998). This approach enables a significant reduction of the sample number without sacrificing the accuracy of calculations. The numerical results of load-displacement diagrams were compared with corresponding laboratory tests performed by Tatsuoka et al (1997). The deterministic calculations for the identical boundary value problem within micro-polar hypoplasticity had already been performed by Tejchman and Herle (1999), Maier (2002), Nübel (2002) and Nübel and Huang (2004). In the last paper, a non-correlated random field of the initial void ratio was generated to promote shear localization. In turn, statistical calculations for other strip footings on sand were carried out, among others, by Fenton and Griffiths (2002) and Niemunis et al (2005). In the first case, the calcu-

lations were carried out in an elastic region. In the second case, the Latin hypercube sampling method was used for a generation of two-dimensional random fields (but not for their classification).

This paper continues the research presented by Tejchman and Górski (2008a, 2008b). In the first paper, deterministic and statistical size effects were investigated during quasi-static shearing of an infinite granular layer between two very rough boundaries under constant vertical pressure using the direct Monte Carlo method and two reduction approaches: stratified sampling and Latin hypercube sampling. These two reduction methods, in contrary to the standard approaches (see e.g. Niemunis et al 2005) were not used for the generation process but for classification of the generated random fields. In turn, in the second paper, calculations with deterministic and statistical size effect were performed in granular specimens subjected to plane strain compression under constant lateral pressure. To estimate the statistical size effect, only Latin hypercube sampling was used. Both calculations have shown that the deterministic size effect was small. The shear resistance at peak and at residual state decreased with increasing ratio of the specimen height h_o and mean grain diameter d_{50}. However, the material ductility, defined as the ratio between the energy consumed during shearing after and before the peak, increased with decreasing h_o/d_{50}. The mean shear resistance at peak with random void ratios was always smaller than this with the same initial mean void ratio. It diminished with increasing h_o/d_{50}. The statistical size effect was always weaker than the deterministic one. For a large standard deviation and weakly correlated fields in both directions, the difference in the friction angle was pronounced: 5° (at peak) and 2° (at the residual state).

The innovations presented in this paper concern the computation of size effects by taking into consideration the effect of pressure which has a pronounced influence on the shear resistance of granular materials. When the pressure level increases, both the friction and dilatancy decrease. As a result, the material strength decreases. Thus, the size effect becomes stronger. For the sake of simplicity, two assumptions were made. First, the calculations were carried out for plane strain. Second, symmetric stochastic fields of initial void ratio were used (in reality they are slightly non-symmetric, Sheppard et al 2006, Aste et al 2007).

The outline of the present paper is as follows. First, after the introduction (Section 1), the laboratory tests performed by Tatsuoka et al (1997) are described briefly (Section 2). Then the employed micro-polar hypoplastic model is summarized (Section 3). The simulation of discrete random fields is described in Section 4. Information about the finite element discretisation and boundary conditions are given in Section 5. The numerical results of the deterministic and statistical size effects are discussed in Section 6. Conclusions are listed in Section 7.

A superposed circle indicates objective time derivation and a superposed dot indicates material time derivation of a particular quantity. Compressive stress and

shortening strain are taken as negative (thus, dilatancy is positive and contractancy is negative).

2. Laboratory Tests

The comprehensive experiments with strip footings of a different width on dense Silver Leighton Buzzard sand (SLB) were performed by Tatsuoka et al (1997). To determine a size effect due to the pressure level and grain size, both the $1g$ and centrifuge tests were performed. In the $1g$ tests, a sand box had the dimensions $24 \times 60 \times 30$ cm^3 (for model footings with a width of B_o = 5 mm, 10 mm and 25 mm) and $40 \times 183 \times 60$ cm^3 (for a model footing with a width of B_o = 100 mm). In the centrifuge tests, a 10×50 cm $\times 30$ cm^3 sand box was used with B_o = 2 cm and 3 cm, respectively. The footing base was made rough by gluing – on a sheet of sand paper. The loading of footings was central. The initial void ratio of sand was $e_o = 0.55$ (initially dense sand).

Figs. 1a and 1b show the relationships between the normalized resultant vertical force $N = 2q/(\gamma_d B_o)$ and normalized vertical displacement s/B_o from $1g$ and centrifuge tests (q – average contact footing pressure). The progressive failure on the basis of local shear strain contours is presented in Fig. 1c (B_o = 100 mm). The result for B_o = 5 mm is erratic (probably due to a low ratio of B_o/d_{50}). The normalized maximum vertical force $N_{\max}$ decreases with increasing B_o ($N_{\max}$ = 350 for B_o = 1.0 cm, $N_{\max}$ = 230 for B_o = 2.5 cm and $N_{\max}$ = 180 for B_o = 5.0 cm). The relationship is hyperbolic (see Fig. 16). The thickness of almost symmetric shear zones beneath the footing is about 6 mm ($10 \times d_{50}$).

In addition, Fig. 2 shows the sand deformations from other experiments with footings on sand (Tatsuoka et al 1991), obtained by means of colored layers. In this case, a complex pattern of non-symmetric shear zones was obtained.

According to Steenfelt (1979), Bätcke (1982), Jarzombek (1989) and Tatsuoka et al (1991, 1997), a deterministic size effect due to the particle size becomes significant for $B_o/d_{50} < 100$–500 (Tatsuoka et al 1991, 1997), $B_o/d_{50} < 100$ (Jarzombek 1989) and $B_o/d_{50} < 33$ (Steenfelt 1979), respectively.

3. Micro-Polar Hypoplastic Model

Despite the discrete nature of granular materials, the mechanical behaviour in a quasi-static regime can be reasonably described by the principles of continuum mechanics. Non-polar hypoplastic constitutive models have been developed at Karlsruhe University (Bauer 1996, Gudehus 1996, von Wolffersdorff 1996), where the stress rate tensor is assured to depend on the stress tensor, strain rate tensor and the void ratio via isotropic nonlinear tensorial functions based on the representation theorem (Wang 1970). The constitutive models were formulated by a heuristic process considering the essential mechanical properties of granular materials undergoing

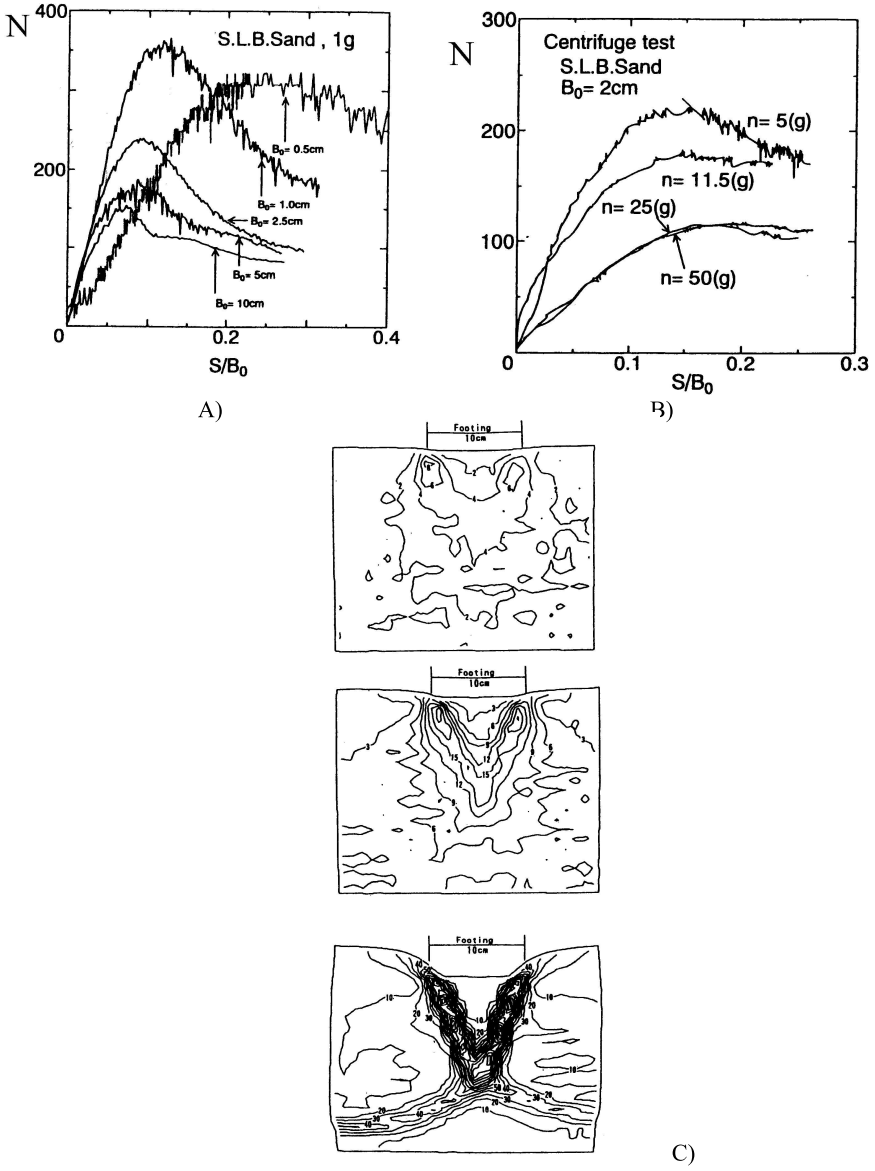

Fig. 1. Evolution of normalised vertical force $N = 2q/(\gamma_d B_o)$ versus normalised vertical displacement S/B_o from $1g$ (A) and centrifuge model tests (B) on SLB sand (q – average contact footing pressure, γ_d – initial unit weight, B_o – footing width) and evolution of local shear strain contours from $1g$ test with footing of B_o = 10 cm (C) (Tatsuoka et al 1997)

homogeneous deformation. They describe the behaviour of so-called simple grain skeletons which are characterised by the following properties:

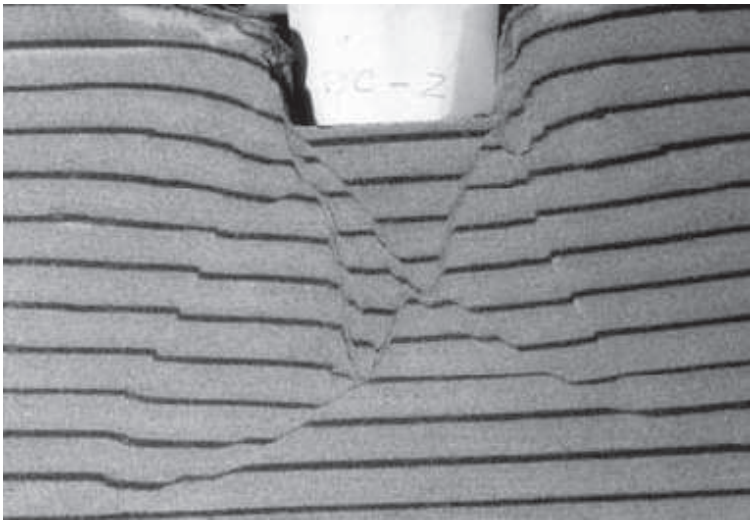

Fig. 2. Sand deformation under footing on sand obtained with colored layers (Tatsuoka et al 1991)

- the state is fully defined through the skeleton pressure and the void ratio (inherent anisotropy of contact forces between grains is not considered and vanishing principal stresses are not allowed),
- deformation of the skeleton is due to grain rearrangements (e.g. small deformations $< 10^{-5}$ due to an elastic behaviour of grain contacts are negligible),
- grains are permanent (abrasion and crushing are excluded in order to keep the granulometric properties unchanged),
- three various void ratios decreasing exponentially with pressure are distinguished (minimum, maximum and critical),
- the material manifests an asymptotic behaviour for monotonous and cyclic shearing or SOM-states for proportional compression,
- rate effects are negligible,
- physico-chemical effects (capillary and osmotic pressure) and cementation of grain contacts are not taken into account.

A striking feature of hypoplasticity is that the constitutive equation is incrementally nonlinear in deformation rate. The hypoplastic models are capable of describing some salient properties of granular materials, e.g. non-linear stress-strain relationship, dilatant and contractant volumetric change, stress level dependence, density dependence and strain softening. A further feature of hypoplastic models is the inclusion of the critical states, i.e. states in which a grain aggregate can deform continuously at constant stress and volume (void ratio). Moreover, both the coaxiality (understood as a coincidence of the directions of the principal stresses and principal plastic strain increments) and stress-dilatancy rule are not defined

(Tejchman and Wu 2008). In contrast to elasto-plastic models, a decomposition of deformation into elastic and plastic parts, the formulation of a yield surface, plastic potential, flow rules and hardening rules are not needed. An exhaustive review of the development of hypoplasticity can be found in Wu and Kolymbas (2000), Tamagnini et al (2000) and Tejchman (2008). The hypoplastic models were initially proposed for cohesionless soil. To increase the application range, a hypoplastic constitutive law has been extended for an elastic strain range (Niemunis and Herle 1997), anisotropy (Tejchman et al 2007) and for viscosity (Niemunis 2003, Gudehus 2006, Tejchman and Wu 2009). It can be also used for soils with low friction angles (Herle and Kolymbas 2004) and clays (Masin, 2005, Huang et al 2006, Weifner and Kolymbas 2008, Masin and Herle 2008). The hallmarks of these models are their simple formulation and procedure for determining material parameters with standard laboratory experiments. The material parameters can be related to the granulometric properties of granular materials, such as grain size distribution curve, shape, angularity and hardness of grains (Herle and Gudehus 1999). A further advantage lies in the fact that one single set of material parameters is valid for a wide range of pressures and densities.

Hypoplastic constitutive models without a characteristic length cannot describe the scale effects associated with shear bands such as thickness and spacing of shear bands. A characteristic length can be introduced into hypoplasticity by means of either the micro-polar, or non-local or second-gradient theory (Maier 2002, Tejchman 2004b). In this paper, a micro-polar theory is adopted. A micro-polar model makes use of rotations and couple stresses, which have clear physical meaning for granular materials. First, the rotations and couple stresses can be observed during shearing and remain negligible during homogeneous deformation (Oda 1993). Second, Pasternak and Mühlhaus (2001) have demonstrated that the additional rotational degree of freedom of a micro-polar continuum arises naturally by mathematical homogenization of an originally discrete system of spherical grains with contact forces and contact moments. In turn, Ehlers et al (2003) have shown that a particle ensemble has the character of a micro-polar Cosserat continuum and the couple stresses naturally result only from the eccentricities of normal contact forces.

A micro-polar continuum considers the deformation at two different levels, i.e.: micro-rotation at the particle level and macro-deformation at the structural level (Schäfer 1962, Mühlhaus 1990). Each material point has, for the case of plane strain, three degrees of freedom: two translations u_i and one independent rotation ω^c. The gradients of the rotation are related to the curvatures $\kappa_i = \omega^c_{,i}$ which are associated with the couple stresses m_i through constitutive equations. The displacements, rotation, stresses and couple stresses in a plane strain micro-polar continuum are shown in Fig. 3. The presence of the couple stresses gives rise to a non-symmetric stress tensor and a characteristic length. Force and moment equilibrium (in static problems, Fig. 3b) require that

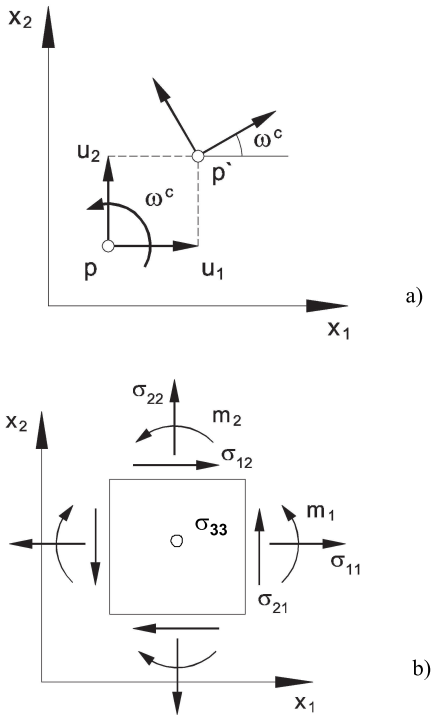

Fig. 3. Plane strain static Cosserat continuum (without body forces and body moment): a) degrees of freedom (u_1 – horizontal displacement, u_2 – vertical displacement, ω^c – Cosserat rotation), b) stresses σ_{ij} and couple stresses m_i at an element

$$\sigma_{11,1} + \sigma_{12,2} - f_1^B = 0, \tag{1}$$

$$\sigma_{21,1} + \sigma_{22,2} - f_2^B = 0, \tag{2}$$

$$m_{1,1} + m_{2,2} + \sigma_{21} - \sigma_{12} - m^B = 0, \tag{3}$$

where σ_{ij} is the stress tensor, m_i denotes the couple stress vector, f_i^B and m^B are the volume body forces and volume body moment, respectively. Eqs. 1–3 are equivalent to the virtual work principle (Mühlhaus 1990, Tejchman and Wu 1993)

$$\begin{aligned} &\int_B (\sigma_{ij}\delta\varepsilon_{ij} + m_i\delta\kappa_i)dV = \\ &= \int_B \left[f_i^B\delta u_i + m^B\delta\omega^c\right]dV + \int_{\partial_1 B} t_i\delta u_i dA + \int_{\partial_2 B} m\delta\omega^c dA, \quad i,j = 1,2, \end{aligned} \tag{4}$$

wherein $t_i = \sigma_{ij}n_j$ and $m = m_i n_i$. t_i and m are prescribed boundary tractions and moment on the boundary $\partial_1 B$ and $\partial_2 B$ with the normal vector n_i. $\delta\varepsilon_{ij}$ and $\delta\kappa_i$ denote

virtual deformations and curvatures, respectively, δu_i are virtual displacements, $\delta\omega^c$ is the virtual Cosserat rotation, A is the surface and V denotes the volume. Virtual displacements and Cosserat rotation vanish on those parts of the boundary where kinematic boundary conditions are prescribed. The virtual work principle (Eq. 4) is used to formulate the FE-equations of motion in a micro-polar continuum (Mühlhaus 1990).

The constitutive relationship between the stress rate, the couple stress rate, the strain rate and the curvature rate can be generally expressed by the following two equations for plane strain (Tejchman and Gudehus 2001):

$$\overset{\circ}{\sigma}_{ij} = F_{ij}(e, \sigma_{kl}, m_i, d^c_{kl}, k_i), \tag{5}$$

$$\overset{\circ}{m}_i = G_i(e, \sigma_{kl}, m_i, d^c_{kl}, k_i). \tag{6}$$

The Jaumann stress rate tensor and Jaumann couple stress rate vector in the above equations are defined by (Mühlhaus 1990)

$$\overset{\circ}{\sigma}_{ij} = \overset{\bullet}{\sigma}_{ij} - w_{ik}\sigma_{kj} + \sigma_{ik}w_{kj} \tag{7}$$

and

$$\overset{\circ}{m}_i = \overset{\bullet}{m}_i - \frac{1}{2}w_{ik}m_k + \frac{1}{2}m_k w_{ki}. \tag{8}$$

The functions F_{ij} and G_i in Eqs. (5) and (6) represent isotropic tensor-valued functions of their arguments; σ_{ij} is the Cauchy stress tensor, m_i is the couple stress vector, e denotes the current void ratio, d^c_{kl} is the polar strain rate and k_i denotes the rate of curvature vector with

$$d^c_{ij} = d_{ij} + w_{ij} - w^c_{ij}, \quad \text{and} \quad k_i = w^c_{,i}. \tag{9}$$

The rate of deformation tensor d_{ij} and the spin tensor w_{ij} are related to the deformation velocity v_i as follows:

$$d_{ij} = \frac{v_{i,j} + v_{j,i}}{2}, \quad w_{ij} = \frac{v_{i,j} - v_{j,i}}{2}, \quad \text{with} \quad ()_{,i} = \frac{\partial()}{\partial x_i}. \tag{10}$$

The rate of Cosserat rotation w^c is defined by

$$w^c_{21} = -w^c_{12} = w^c \quad \text{and} \quad w^c_{kk} = 0. \tag{11}$$

For moderate stress levels, the grains of granular materials can be reasonably assumed to be incompressible. In this case, the change of void ratio depends only on the strain rate:

$$\overset{\bullet}{e} = (1+e)d_{kk}. \tag{12}$$

For the numerical calculations, the following micro-polar hypoplastic constitutive equations are considered (Tejchman and Gudehus 2001):

$$\overset{\circ}{\sigma}_{ij} = f_s \left[L_{ij}\left(\hat{\sigma}_{kl}, \hat{m}_k, d^c_{kl}, k_k d_{50}\right) + f_d N_{ij}\left(\hat{\sigma}_{ij}\right) \sqrt{d^c_{kl} d^c_{kl} + k_k k_k d^2_{50}} \right] \tag{13}$$

and

$$\frac{\overset{\circ}{m}_i}{d_{50}} = f_s \left[L^c_i\left(\hat{\sigma}_{kl}, \hat{m}_k, d^c_{kl}, k_k d_{50}\right) + f_d N^c_i\left(\hat{m}_i\right) \sqrt{d^c_{kl} d^c_{kl} + k_k k_k d^2_{50}} \right], \tag{14}$$

wherein the normalized stress tensor $\hat{\sigma}_{ij}$ is defined by

$$\hat{\sigma}_{ij} = \frac{\sigma_{ij}}{\sigma_{kk}}, \tag{15}$$

and the normalized couple stress vector $\hat{m}_i$ is defined by

$$\hat{m}_i = \frac{m_i}{\sigma_{kk} d_{50}}, \tag{16}$$

wherein d_{50} is the mean grain diameter of sand. The scalar factors $f_s = f_s(e, \sigma_{kk})$ and $f_d = f_d(e, \sigma_{kk})$ in Eqs. (13) and (14) describe the influence of density and stress level on the incremental stiffness. The factor f_s depends on the granulate hardness h_s, the mean stress σ_{kk}, the maximum void ratio e_i and the current void ratio e through the following relationship (Bauer 1996)

$$f_s = \frac{h_s}{n h_i} \left(\frac{1+e_i}{e_i} \right) \left(\frac{e_i}{e} \right)^{\beta} \left(-\frac{\sigma_{kk}}{h_s} \right)^{1-n}, \tag{17}$$

with

$$h_i = \frac{1}{c_1^2} + \frac{1}{3} - \left(\frac{e_{i0} - e_{d0}}{e_{c0} - e_{d0}} \right)^{\alpha} \frac{1}{c_1 \sqrt{3}}. \tag{18}$$

In the above equations, the granulate hardness h_s represents a reference pressure similar to the atmospheric pressure, the coefficients α and β express dependence on density and stress level respectively, and n denotes the compression coefficient. The multiplier f_d represents the dependence on the relative density:

$$f_d = \left(\frac{e - e_d}{e_c - e_d} \right)^{\alpha}. \tag{19}$$

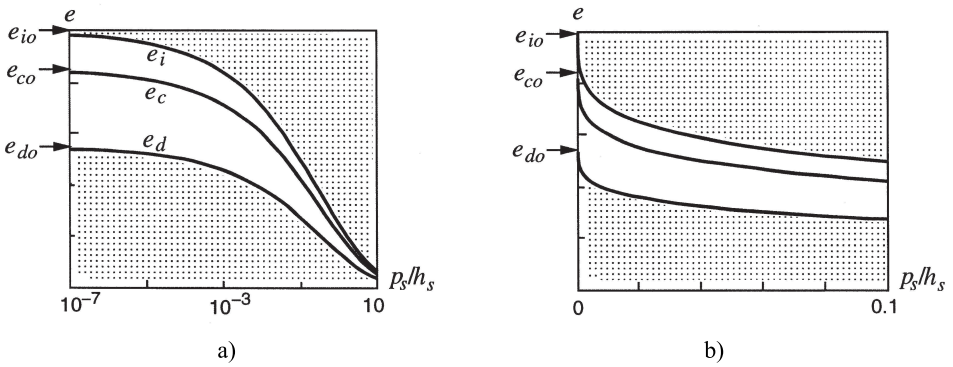

Fig. 4. Relationship between void ratios e_i, e_c and e_d and mean pressure p_s in a logarithmic (a) and linear (b) scale (grey zones denote inadmissible states)

The relative density in the above expression involves the void ratio in critical state e_c, the minimum void ratio e_d (the densest packing) and the maximum void ratio e_i (the loosest packing). In a critical state, granular material experiences continuous deformation while the stress and void ratio remain unchanged. The current void ratio e is bounded by the two extreme void ratios e_i and e_d (Fig. 4). Based on experimental observations, the void ratios e_i, e_d and e_c are assumed to depend on the stress level σ_{kk} through the following affine relationships (Bauer 1996):

$$e_i = e_{i0} \exp\left[-\left(-\frac{\sigma_{kk}}{h_s}\right)^n\right], \tag{20}$$

$$e_d = e_{d0} \exp\left[-\left(-\frac{\sigma_{kk}}{h_s}\right)^n\right], \tag{21}$$

$$e_c = e_{c0} \exp\left[-\left(-\frac{\sigma_{kk}}{h_s}\right)^n\right], \tag{22}$$

wherein e_{i0}, e_{d0} and e_{c0} are the values of e_i, e_d and e_c at $\sigma_{kk} = 0$, respectively.

For the functions L_{ij}, N_{ij}, L_i^c and N_i^c in the constitutive Eqs. (13) and (14), the following specific expressions are used (Tejchman and Gudehus 2001):

$$L_{ij} = a_1^2 d_{ij}^c + \hat{\sigma}_{ij}\left(\hat{\sigma}_{kl} d_{kl}^c + \hat{m}_k k_k d_{50}\right), \tag{23}$$

$$L_i^c = a_1^2 k_i d_{50} + a_1^2 \hat{m}_i\left(\hat{\sigma}_{kl} d_{kl}^c + \hat{m}_k k_k d_{50}\right), \tag{24}$$

$$N_{ij} = a_1\left(\hat{\sigma}_{ij} + \hat{\sigma}_{ij}^*\right), \tag{25}$$

$$N_i^c = a_1^2 a_c \hat{m}_i, \tag{26}$$

where

$$a_1^{-1} = c_1 + c_2 \sqrt{\hat{\sigma}^*_{kl}\hat{\sigma}^*_{lk}}\,[1 + \cos(3\theta)]\,, \tag{27}$$

$$\cos(3\theta) = -\frac{\sqrt{6}}{\left[\hat{\sigma}^*_{pq}\hat{\sigma}^*_{pq}\right]^{1.5}}\left(\hat{\sigma}^*_{kl}\hat{\sigma}^*_{lm}\hat{\sigma}^*_{mk}\right), \tag{28}$$

with

$$c_1 = \sqrt{\frac{3}{8}}\frac{(3-\sin\phi_c)}{\sin\phi_c}, \quad c_2 = \frac{3}{8}\frac{(3+\sin\phi_c)}{\sin\phi_c}. \tag{29}$$

The material constant ϕ_c is the friction angle in critical state and the stress function θ denotes the Lode angle in the deviatoric plane at $\hat{\sigma}_{ii} = 1$ (calculated with a symmetric stress tensor), and $\hat{\sigma}^*_{ij}$ denotes the deviatoric part of $\hat{\sigma}_{ij}$. The micro-polar parameter a_c in Eq. (26) can be correlated with the grain roughness. This correlation can be established by studying the shearing of a narrow granular strip between two rough boundaries (Tejchman and Gudehus 2001). It can be represented by a constant, $a_c = 1 \div 5$, or connected to the parameter a_1^{-1}, $a_c = (0.5 \div 1.5) \times a_1^{-1}$. The parameter a_1^{-1} (Eq. 27) lies in the range of 3.0–4.3 for the usual range of critical friction angle.

In general, the above constitutive model requires the following ten material parameters: e_{i0}, e_{d0}, e_{c0}, ϕ_c, h_s, β, n, α, a_c and d_{50} (nine material parameters if $a_c = f(a_1)$). They were calibrated for a pressure range of 1 kPa$< p_s = -\sigma_{kk}/3 <$ 1000 kPa. Below it, additional capillary forces due to the air humidity and van der Waals forces may become important, and above it, grains are crushing. The calibration procedure for non-polar material parameters in the case of different sands (0.1 mm $\le d_{50} \le$ 2.0 mm, $1.4 \le C_u \le 7.2$, C_u – coefficient of uniformity) was given in detail by Bauer (1996), Herle and Gudehus (1999) and Rondon et al (2007). The parameters h_s and n can be estimated from a single oedometric compression test with an initially loose specimen (h_s reflects the slope of the curve in a semi-logarithmic representation, and n its curvature). The parameters α and β can be determined from a triaxial or plane strain test with a dense specimen. The critical friction angle ϕ_c can be determined from the angle of repose or measured in a triaxial test with a loose specimen. The parameters of e_{i0}, e_{d0}, e_{c0} and d_{50} are obtained from conventional index tests ($e_{c0} \approx e_{\max}$, $e_{d0} \approx e_{\min}$, $e_{i0} \approx (1.1 - 1.5)e_{\max}$).

The FE-analyses were carried out with the following material constants for SLB sand: $e_{i0} = 0.86$, $e_{d0} = 0.51$, $e_{c0} = 0.79$, $\phi_c = 29°$, $h_s = 300$ MPa, $\beta = 1$, $n = 0.40$,

$\alpha = 0.16$, $a_c = a_1^{-1}$ and $d_{50} = 0.60$ mm (Tejchman and Herle 1999). It should be noted that the calibration of the material parameters was not performed by following the standard procedure described above. First, the required laboratory calibration tests were performed, and second, the material parameters were found by fitting element test calculations with results of plane strain compression tests without taking into account shear localization.

The capability of a micro-polar hypoplastic constitutive model of solving different boundary value problems including shear localization was verified, among others, by Tejchman and Bauer (1996), Tejchman and Gudehus (2001), Tejchman and Niemunis (2006), Tejchman and Wu (2009), Tejchman and Górski (2008), Gudehus and Nübel (2004), Nübel and Huang (2004), and Tejchman (2008). A satisfactory agreement between numerical and experimental results was achieved in particular for monotonic and cyclic symmetric deformation (Tejchman 2008). However, the model shows evident shortcomings for deformation with small amplitudes since an excessive accumulation of deformation (called ratchetting) occurs. To avoid it, the model has to be extended by including intergranular strain (Niemunis and Herle 1997).

4. FE-Input Data

4.1. Deterministic Calculations

The FE-calculations of a footing on sand (assuming a uniform distribution of the initial void ratio e_o) were performed with 3 different footing widths ($B_o = 1.0$ cm, 2.5 cm and 5.0 cm) for a granular specimen of $b_o \times h_o = 60 \times 24$ cm^2 (b_o – initial width, h_o – initial height). The specimen depth was equal to l=1.0 m due to plane strain conditions. In all cases, quadrilateral finite elements divided into 6212 triangular elements were used (Fig. 5). Quadrilateral elements composed of four diagonally crossed triangles were used to avoid volumetric locking due to dilatancy effects (Groen 1997). Linear shape functions were used for displacements and for the Cosserat rotation. The integration was performed with one sampling point placed in the middle of each element. To properly capture shear localization inside of the granular specimen, the size of the triangular finite elements s_e was not larger than five mean grain diameters d_{50} (Tejchman and Bauer 1996). This condition was fulfilled close to the footing in the area 'A' of 6×12 cm^2, where $s_e = 2.5$ mm = $4.2 \times d_{50}$ (Fig. 5). As mentioned earlier, during calculations, the effect of pressure was taken into account in the micro-polar hypoplastic model.

A quasi-static deformation in sand was imposed through a constant vertical displacement increment Δu prescribed at nodes along the very rough footing. To simulate this roughness, the horizontal displacement and Cosserat rotation along the footing were assumed to be equal to zero. For this reason, the edges of the box containing sand were very smooth. The vertical displacement increments were chosen as $\Delta u/B_o = 0.000025$–0.000050. About 20000–30000 steps were performed.

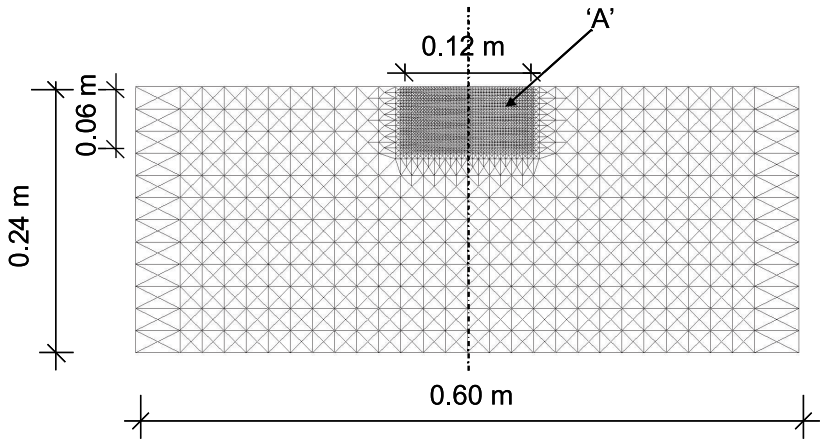

Fig. 5. FE-mesh used for plane strain calculations

As an initial stress state, a K_0-state with $\sigma_{22} = \gamma_d x_2$ and $\sigma_{11} = K_0 \gamma_d x_2$ was assumed in the specimen; x_2 is the vertical coordinate measured from the top of the specimen, $\gamma_d = 17.0$ kN/m^3 denotes the initial volumetric weight and $K_0 = 0.50$ is the earth pressure coefficient at rest (σ_{11} – horizontal normal stress, σ_{22} – vertical normal stress). The initial void ratio was $e_o = 0.55$.

For the solution of a non-linear equation system, a modified Newton-Raphson scheme with line search was used. The global stiffness matrix was calculated with only linear terms of the constitutive equations (Eqs. 23 and 24). In order to accelerate the convergence in the softening regime, the initial increments of displacements and Cosserat rotations in each calculation step were assumed to be equal to the final increments in the previous step. The procedure was found to yield sufficiently accurate solutions with a fast convergence. Due to non-linear terms in deformation rate and material softening, this procedure turned out to be more efficient than a full Newton-Raphson method (Tejchman 2008). The iteration steps were performed using translational and rotational convergence criteria. For the time integration of stresses in finite elements, a one-step Euler forward scheme was applied. The calculations were carried out with large deformations and curvatures using a so-called "Updated Lagrangian" formulation by taking into account the Jaumann stress rate and Jaumann couple stress rate and the actual shape and area of finite elements.

4.2. Statistical Calculations

To generate the random fields, a conditional-rejection method was applied (Walukiewicz et al 1997). The method makes it possible to simulate any homogeneous fields for which the expected value and variance are constant (Knabe et al 1998, Vanmarcke 1983) or non-homogeneous truncated Gaussian random fields described on a regular or irregular two dimensional spatial mesh. The input data of the method are: a correlation function $K(x, y)$, mean values, standard deviations, and

in the case of a truncated field – the truncation parameter. Using the correlation function $K(x, y)$, the covariance matrix $\mathbf{K}$ defined in discrete points of the mesh is calculated. First, several random points are generated with the help of a standard unconditional generation method (Walukiewicz et al 1997). Then, the conditional version of the algorithm is used, which allows for a generation of the next group of random values. The method is of a sequential type. A "base scheme" is defined which covers a limited mesh area (hundred points), and only these points are used in the calculations of the next random values. The base scheme is appropriately shifted to cover all the field nodes. The proposed approach allows for a generation of practically unlimited random fields (thousands of discrete points). Here, only a short description of the conditional version of the method is provided. Using this algorithm, a single random vector, described on the defined base scheme, can be generated:

1. Determination of the local covariance matrix $\mathbf{K}$, the unknown $\mathbf{X}_u$ and known part of the random vector $\mathbf{X}_k$ and the expected values vector $\overline{\mathbf{X}}$:

$$\mathbf{X} = \left\{ \begin{array}{c} \mathbf{X}_u \\ \mathbf{X}_k \end{array} \right\}, \qquad \mathbf{K} = \left[\begin{array}{cc} \mathbf{K}_{11} & \mathbf{K}_{12} \\ \mathbf{K}_{21} & \mathbf{K}_{22} \end{array} \right], \quad \overline{\mathbf{X}} = \left\{ \begin{array}{c} \overline{\mathbf{X}}_u \\ \overline{\mathbf{X}}_k \end{array} \right\}. \tag{30}$$

2. Determination of the conditional variance matrix $\mathbf{K}_c$ and the conditional mean vector $\overline{\mathbf{X}}_c$:

$$\mathbf{K}_c = \mathbf{K}_{11} - \mathbf{K}_{12}\mathbf{K}_{22}^{-1}\mathbf{K}_{21}, \tag{31}$$

$$\overline{\mathbf{X}}_c = \overline{\mathbf{X}}_u + \mathbf{K}_{12}\mathbf{K}_{22}^{-1}\left(\mathbf{X}_k - \overline{\mathbf{X}}_k\right). \tag{32}$$

3. Determination of the maximal value of the density function $f_{\max}$

$$f_{\max} = (1-t)^{-n/2}(\det \mathbf{K}_c)^{-n/2}(2\pi)^{-n/2} \times (2\mathrm{erf}(s))^{-n}, \tag{33}$$

$$t = \frac{s \times \exp\left(-\frac{s^2}{2}\right)}{\sqrt{2\pi}\ \mathrm{erf}(s)}, \quad s \geq 0 \quad \text{and} \quad \mathrm{erf}(s) = \frac{1}{2\pi}\int_0^s \exp\left(-\frac{x^2}{2}\right) dx, \tag{34}$$

where t and s are the truncation parameters.

4. Generation of the vector of unknown values $\mathbf{X}_u$:

$$X_i = a_i + (b_i - a_i)\, u_i \qquad i = 1, \ldots, n, \tag{35}$$

where u_i is a random variable uniformly distributed in the interval [0,1]. The intervals (a_i, b_i) are defined for all points of the mesh and establish an envelope of the random field. The envelope specifies the characteristic features of the field

under consideration, for example, their maximal and minimal values. It can be given in the form of a function or by an experimental discrete data.

5. Calculation of the conditional density function $f(\mathbf{X}_u)$:

$$f\left(\mathbf{X}_u\right) = f_{\max} \exp\left(-0.5 J\left(\mathbf{X}_u\right)\right), \tag{36}$$

where

$$J\left(\mathbf{X}_u\right) = \frac{1}{2(1-t)} \left(\mathbf{X}_u - \overline{\mathbf{X}}_c\right)^T \mathbf{K}_c^{-1} \left(\mathbf{X}_u - \overline{\mathbf{X}}_c\right). \tag{37}$$

6. Generation of the independent random variable u_{n+1} from the interval [0, 1] and checking the condition

$$f_{\max} u_{n+1} \leq f\left(\mathbf{X}_u\right). \tag{38}$$

7. If this condition holds, the random value $\mathbf{X}_u$ is accepted; if not, the calculation returns to the point 4.

To describe the discrepancies between the theoretical and generated fields, the following global G_{er} and local V_{er} (variance) errors are calculated (Walukiewicz et al 1997):

$$G_{er}\left(\mathbf{K},\ \hat{\mathbf{K}}\right) = \frac{\left|\|\mathbf{K}\| - \left\|\hat{\mathbf{K}}\right\|\right|}{\|\mathbf{K}\|} \times 100\%, \tag{39}$$

$$V_{er}\left(k_{ii}, \hat{k}_{ii}\right) = \sum_{i=1}^{m} \frac{\left(k_{ii} - \hat{k}_{ii}\right)}{\left(k_{ii}\right)} \times 100\%, \tag{40}$$

where $\hat{\mathbf{K}}$ is the estimator of the covariance matrix $\mathbf{K}$ calculated with the help of the generated fields

$$\hat{\mathbf{K}} = \frac{1}{NR-1} \sum_{i=1}^{NR} \left(\hat{\mathbf{X}}_i - \overline{\hat{\mathbf{X}}}\right)\left(\hat{\mathbf{X}}_i - \overline{\hat{\mathbf{X}}}\right)^T, \qquad \overline{\hat{\mathbf{X}}} = \frac{1}{NR} \sum_{i=1}^{NR} \hat{\mathbf{X}}_i. \tag{41}$$

The parameter $\hat{\mathbf{X}}$ is the estimator of the random vector $\mathbf{X}$, and $\overline{\hat{\mathbf{X}}}$ is the estimator of its mean value, NR denotes the number of realizations, $\|\mathbf{K}\| = \sqrt{tr\left(\mathbf{K}\right)^2}$ is the matrix norm, k_{ii} and $\hat{k}_{ii}$ denote the diagonal element of the covariance matrix $\mathbf{K}$ and its estimators $\hat{\mathbf{K}}$, respectively.

In the work, the Monte Carlo method is applied. The following steps are required:

– simulation of random variables or fields describing the problem under consideration, for example, variability of material parameters, initial imperfections in structure geometrics and others,
– solution of the problem for each simulated realization and creation of a set of results,
– statistical description of the obtained set of results.

Contrary to stochastic finite element codes, the Monte Carlo method does not impose any restriction onto the solved random problems. Linear or nonlinear problems can be analysed using standard commercial deterministic programs without any improvements or modifications. The only limitation of the method is calculation time. For example, to reproduce exactly the input random data of shell initial geometric imperfections, at least 2000 random samples should be used (Bielewicz and Górski 2002). Any nonlinear calculations for such a number of initial data are, however, impossible due to excessive computation times. To determine a minimal but sufficient number of samples which allows one to estimate the results with a desired accuracy, a convergence analysis of the results has been proposed (Górski 2006). It has been estimated that in the case of the shell initial geometric imperfections only about 50 realizations need be considered. A further decrease of sample numbers can be obtained using Monte Carlo reduction methods. In the paper by Tejchman and Górski (2008), two methods were considered: a stratified and a Latin sampling method. These methods were not used for the generation of two-dimensional random fields, but for their classification. For that reason, a single realization was generated according to the initial data, i.e. the mean value and the covariance matrices were exactly reproduced. The calculations have shown (Tejchman and Górski 2008a) that using these reduction methods, the results can be properly estimated by several realizations (e.g. 12–15).

Various properties of granular bodies may be considered as randomly distributed: e.g. initial stresses (Niemunis et al 2005), mean grain diameter (Górski et al 2008), initial void ratio (Gudehus and Nübel 2004). In the present work, only fluctuations of void ratio were taken into account (as proposed by Gudehus and Nübel 2004). Randomness of the initial void ratio e_o should be described by a correlation function. For lack of the appropriate data, the correlation function is usually chosen arbitrarily. It is obvious that the fluctuation of any material parameters should be described by a homogeneous function. Furthermore, the function should confirm that the correlation between random material variables vanishes when the random point distance increases. Any non-homogeneous correlation function, e.g. Wiener or Brown function (Vanmarcke 1983) defines strong correlation between every point of the field, and such description of material parameters is unrealistic. The simplest choice is a standard first order anisotropic correlation function $K(\Delta x_1, \Delta x_2) = e^{-\lambda_{x_1}\Delta x_1} e^{-\lambda_{x2}\Delta x_2}$. Here, the following, more general, second order, homogeneous correlation function was adopted (Bielewicz and Górski 2002):

$$K(\Delta x_1, \Delta x_2) = s_{e_o}^2 \times e^{-\lambda_{x_1}\Delta x_1}(1 + \lambda_{x_1}\Delta x_1)e^{-\lambda_{x_2}\Delta x_2}(1 + \lambda_{x_2}\Delta x_2), \tag{42}$$

where Δx_1 and Δx_2 are the distances between two field points along the horizontal axis x_1 and vertical axis x_2, λ_{x1} and λ_{x2} are the decay coefficients (damping parameters) characterizing a spatial variability of the specimen properties (i.e. describe the correlation between the random field points), while the standard deviation s_{e_o} represents the field scattering.

It is possible to compare the two homogeneous functions using the scale of fluctuation θ (average length of the correlation distance, Vanmarcke (1983)). For the normalized function (Eq. 42) $\theta = 4/\lambda$ (with $\Delta x \to 0$) and the parameter is twice as big as the fluctuation scale of a standard first order correlation function (Vanmarcke 1983). Thus, by using appropriate decay coefficients λ, in this case, the second order correlation function can be approximated by the first order one. The second order homogeneous function (Eq. 42) proved to be very useful when the conditional-rejection method of generation was applied (Knabe et al 1998).

In finite element methods, continuous correlation function (Eq. 42) must be represented by the appropriate covariance matrix (Eq. 30). For this purpose, the procedure of local averages of the random fields proposed by Vanmarcke (1983) was adopted. After an appropriate integration of the function (Eq. 42), the following expressions describing the variances D_w and covariances K_w were obtained (Knabe et al 1998):

$$\begin{aligned} D_w(\Delta x_1, \Delta x_2) = {} & \frac{2}{\lambda_{x_1}\Delta x_1} s_{e_o}^2 \left[2 + e^{-\lambda_{x_1}\Delta x_1} - \frac{3}{\lambda_{x_1}\Delta x_1}\left(1 - e^{-\lambda_{x_1}\Delta x_1}\right)\right] \times \\ & \times \frac{2}{\lambda_{x_2}\Delta x_2}\left[2 + e^{-\lambda_{x_2}\Delta x_2} - \frac{3}{\lambda_{x_2}\Delta x_2}\left(1 - e^{-\lambda_{x_2}\Delta x_2}\right)\right], \end{aligned} \tag{43}$$

$$\begin{aligned} K_w(\Delta x_1, \Delta x_2) = {} & \frac{e^{\lambda_{x_1}\Delta x_1}}{(\lambda_{x_1}\Delta x_1)^2} s_{e_o}^2 \{[\cos(\lambda_{x_1}\Delta x_1) - \sin(\lambda_{x_1}\Delta x_1)] + 2\lambda_{x_1}\Delta x_1 - 1\} \times \\ & \times \frac{e^{\lambda_{x_2}\Delta x_2}}{(\lambda_{x_2}\Delta x_2)^2} s\{[\cos(\lambda_{x_2}\Delta x_2) - \sin(\lambda_{x_2}\Delta x_2)] + 2\lambda_{x_2}\Delta x_2 - 1\}. \end{aligned} \tag{44}$$

In our stochastic calculations, a mean initial void ratio of $\bar{e}_0 = 0.55$ was assumed. We took into account a weak correlation of the initial void ratio e_o in both directions ($\lambda_{x1} = 3$ and $\lambda_{x2} = 3$ in Eqs. 43 and 44) and its high standard deviation equal to $s_{e_o} = 0.10$. The range of significant correlation was approximately 40 mm. The following constant intervals of the mesh points were applied: $a_i = b_i = 0.09$ (Eq. 35). In this way, the initial void ratio changed between 0.44 and 0.64. The dimension of the random field was the same as the finite element mesh in the area

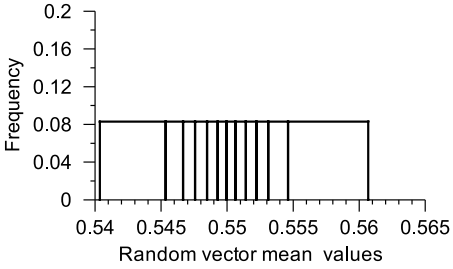

Fig. 6. Stratified sampling method for footings on sand

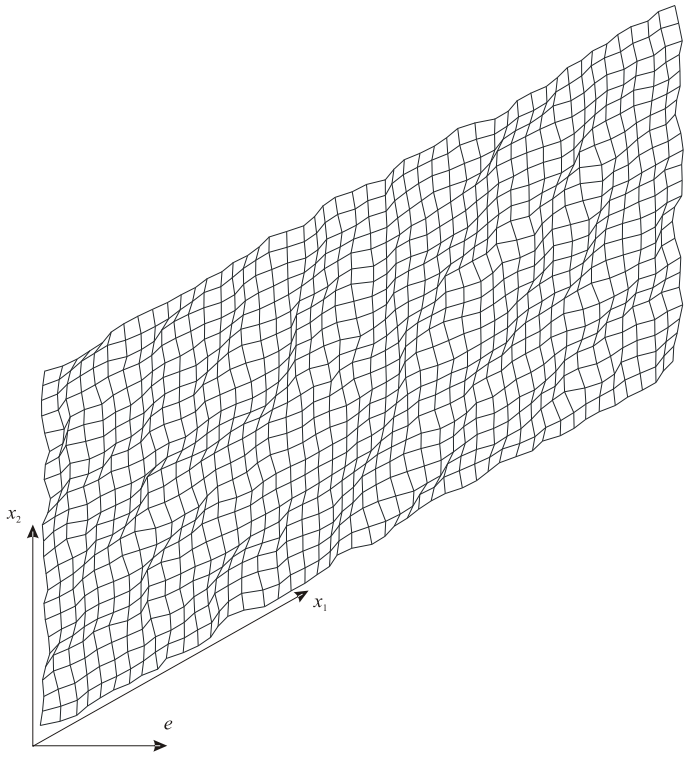

Fig. 7. Stochastic distribution of initial void ratio close to the footing (area 'A' of Fig. 5) in one granular specimen

'A' (Fig. 5). Only $24 \times 48 = 1152$ initial random void ratios were generated, one value for one quadrilateral finite element. The same random values were assumed in 4 neighbouring triangular elements. Using the algorithm described above in Section 3, 2000 field realizations of the initial void ratio were generated. The global G_{er} and local (variance) V_{er} errors of the generation were calculated (Eqs. 39 and 40): $G_{er} = 2.34\%$, $V_{er} = 0.14\%$.

According to the stratified sampling method, the realizations of the random field were chosen in a strictly defined manner. First, the generated samples were classified and arranged in increasing order according to the chosen parameter (e.g. their mean values). Then, the variable domain was divided into 12 intervals of equal probability. On this basis, their distributions were specified in the form of histogram (Fig. 6). From each interval, only one realization close to the centre of the subfield was used as the input data to the FEM calculations. In this way, the results of 12 realizations were analyzed.

Fig. 7 shows a stochastic distribution of the initial void ratio in one granular specimen in the area 'A' of Fig. 5. The initial void ratio changes in the entire region between 0.44 and 0.64. Due to the fact that the initial void ratio scattering in the specimen is limited by the pressure dependent void ratios $e_{i0} = 0.86$ (upper bound, Eq. 21) and $e_{d0} = 0.51$ (lower bound, Eq. 22), the initial values of e_o below 0.51 were simply cut off at the beginning of calculations. For comparison, the statistical calculations were also performed with $e_{d0} = 0.44$ (only for $B_o = 2.5$ cm). In this case, initial void ratios were not cut off below e_{d0}.

5. FE-Results

5.1. Deterministic Size Effect

Fig. 8 shows the evolution of the calculated normalized vertical force $N = 2q/(\gamma_d B_o) = 2P/(\gamma_d B_o^2)$ (q – average contact footing pressure) for three different footing widths B_o: 10 mm, 25 mm and 50 mm on initially dense SLB sand with a uniform distribution of initial void ratio with $e_o = 0.55$. In addition, a distribution of void ratio e

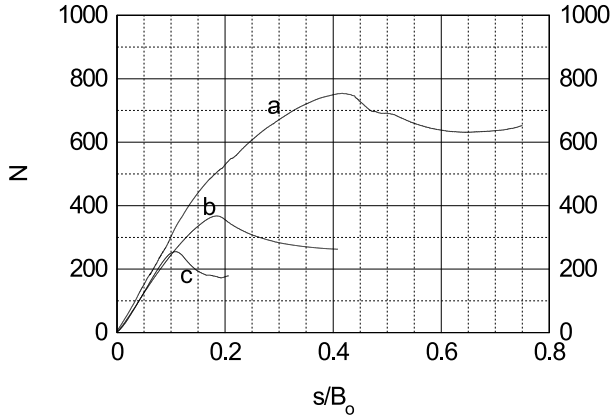

Fig. 8. Evolution of normalised vertical force $N = 2q/(\gamma_d B_o)$ versus normalised vertical displacement s/B_o from FE-calculations with uniform distribution of $e_o = 0.55$ (q – average contact footing pressure, γ_d – initial unit weight, B_o – footing width): a) $B_o = 1$ cm, b) $B_o = 2.5$ cm, c) $B_o = 5$ cm

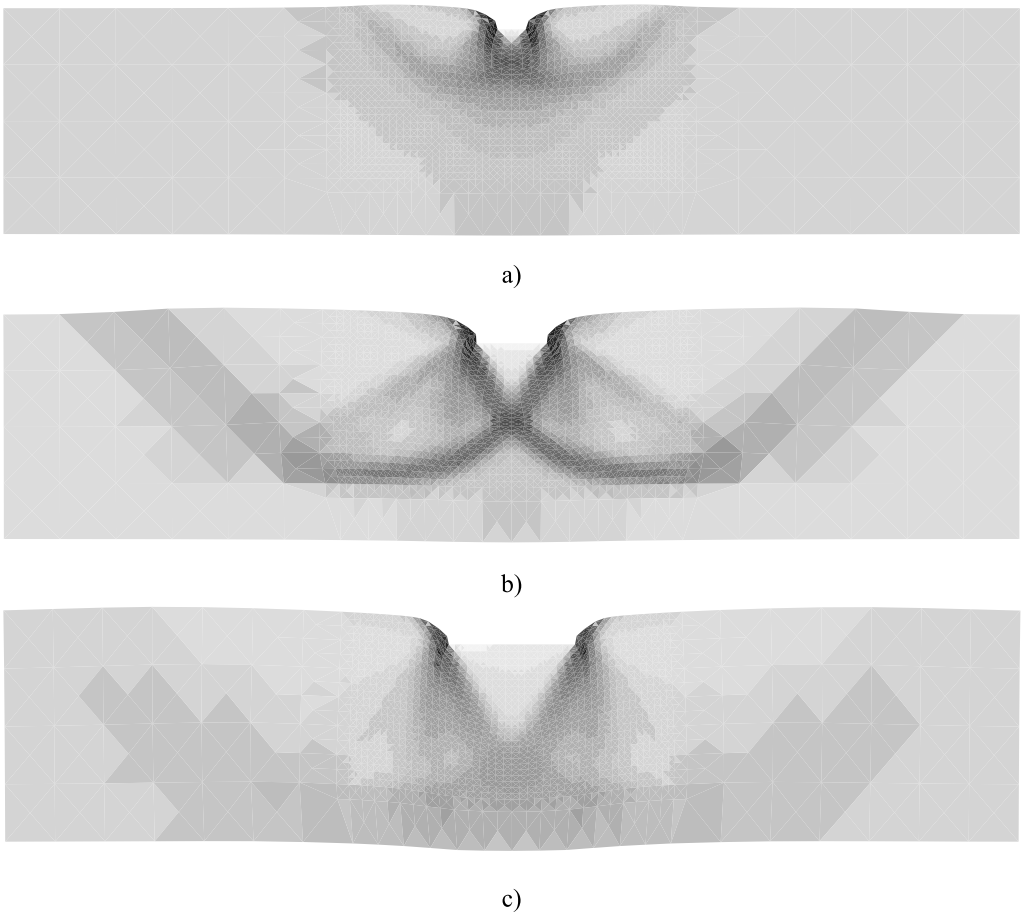

Fig. 9. Distribution of void ratio close to the footing from FE calculations with uniform distribution of $e_o = 0.55$: a) $B_o = 1.0$ cm, b) $B_o = 2.5$ cm, c) $B_o = 5.0$ cm

at residual state is shown close to footings (Fig. 9) (the darker the color, the higher the void ratio). The vertical force was calculated as the total sum of vertical forces at the nodes along the footing.

The resultant normalized vertical force on the footing at first increases, shows a pronounced peak and later drops, then reaching approximately its residual value. Its maximum value increases with decreasing footing width. As compared to experiments, the calculated vertical force $N_{\max}$ is too high, in particular for $B_o = 1.0$ cm ($N_{\max} = 750$ for $B_o = 1.0$ cm, $N_{\max} = 360$ for $B_o = 2.5$ cm and $N_{\max} = 254$ for $B_o = 5$ cm). The normalized vertical footing displacement corresponding to the peak grows with decreasing specimen size (from 10% up to 40%). According to (Nübel and Huang 2004), a significant decrease of the maximum vertical force on the footing can be achieved by decreasing wall friction between sand and footing. However, our calculations have shown that the maximum vertical force diminishes

for a smooth footing by only 20%. A more accurate calibration procedure of material parameters is needed.

The calculated deformation field close to the footing (Fig. 9) is in good accordance with the experiment (Fig. 1). During the footing displacement, first, a stiff wedge of sand is created beneath the point at which the material undergoes slight densification. Below the edge, two symmetric parabolic shear zones occur, which are manifested by significant dilatancy, i.e. increase of void ratio.

The deterministic size effect could be approximately taken into account by a change of initial void ratio, i.e. the higher the pressure level, the higher should be the initial void ratio. The behaviour of initially dense sand at high pressures corresponds to the behaviour of initially medium sand at low pressures. The scaling law for the initial void ratio could be determined with several comparative numerical simulations with different B_o and e_o.

5.2. Statistical Size Effect

The evolutions of the normalized vertical force N versus normalized vertical displacement s/B_o are shown in Fig. 10 for 3 different footing widths B_o. The distribution of void ratio close to the footing for six arbitrarily selected distributions of the initial void ratio (cases No. '2', '3', '6', '7', '11' and '12' of Fig. 6) are shown in Fig. 11 at the residual state (B_o = 2.5 cm, s/B_o = 0.4–0.6). In turn, Fig. 12 demonstrates the distribution of the Cosserat rotation close to the footing (indicated by circles) at the residual state (s/B_o = 0.6) for one granular specimen (case No. '2' of Fig. 6). In addition, for this last case, the distribution of void ratio is depicted for two different footing displacements s/B_o (Fig. 13).

The effect of the distribution of the initial void ratio is significant. The mean normalized vertical force $N_{\max}$ decreases obviously with decreasing footing width B_o. For B_o = 1 cm, it is higher ($N_{\max}$ = 775) than the deterministic value ($N_{\max}$ = 750). If B_o = 2.5 cm, it is similar ($N_{\max}$ = 360). However, for B_o = 5 cm, it is smaller ($N_{\max}$ = 238) than the deterministic value ($N_{\max}$ = 254). The deformation field can be strongly non-symmetric including several curved and straight shear zones (Figs. 11 and 12). Shear localization is characterized by the presence of Cosserat rotation and an increase of the void ratio. The thickness of the curved shear zone under the footing on the basis of the deformed mesh is about $12 \times d_{50}$ (it includes 3 elements subjected to shear deformation) (Fig. 12). Outside the area 'A' (Fig. 8), the thickness of shear zones becomes wider due to overly large mesh elements. The void ratio approaches, in shear zones, its pressure-dependent residual value (Eq. 22). The number, shape and placement of shear zones are very sensitive to the distribution of e_o. The curved shear zones develop after the peak (s/B_o = 0.2), and they are well noticeable at s/B_o = 0.3 (Fig. 13). The deformation fields of Fig. 11 are qualitatively similar to the experimental one (Fig. 2).

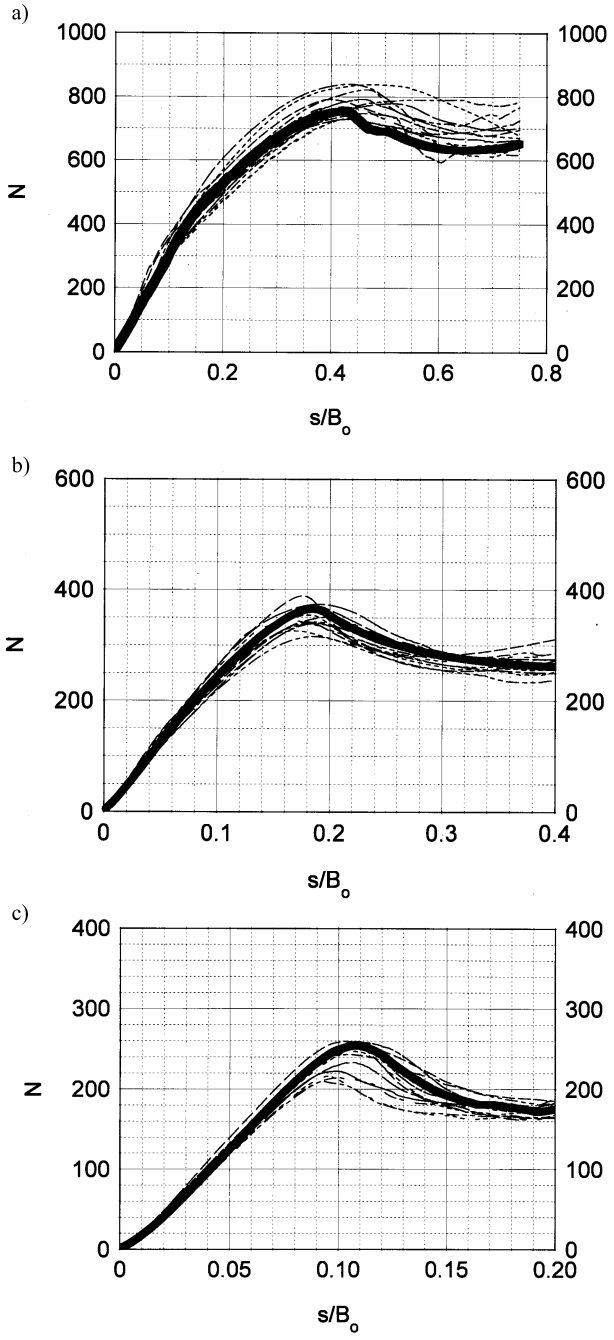

Fig. 10. Evolution of normalised vertical force $N = 2q/(\gamma_d B_o)$ versus normalised vertical displacement s/B_o from FE-calculations with uniform (thick solid line) and random distribution of e_o (dotted lines): a) $B_o = 1.0$ cm, b) $B_o = 2.5$ cm, c) $B_o = 5.0$ cm (q – average contact footing pressure, γ_d – initial unit weight, B_o – footing width)

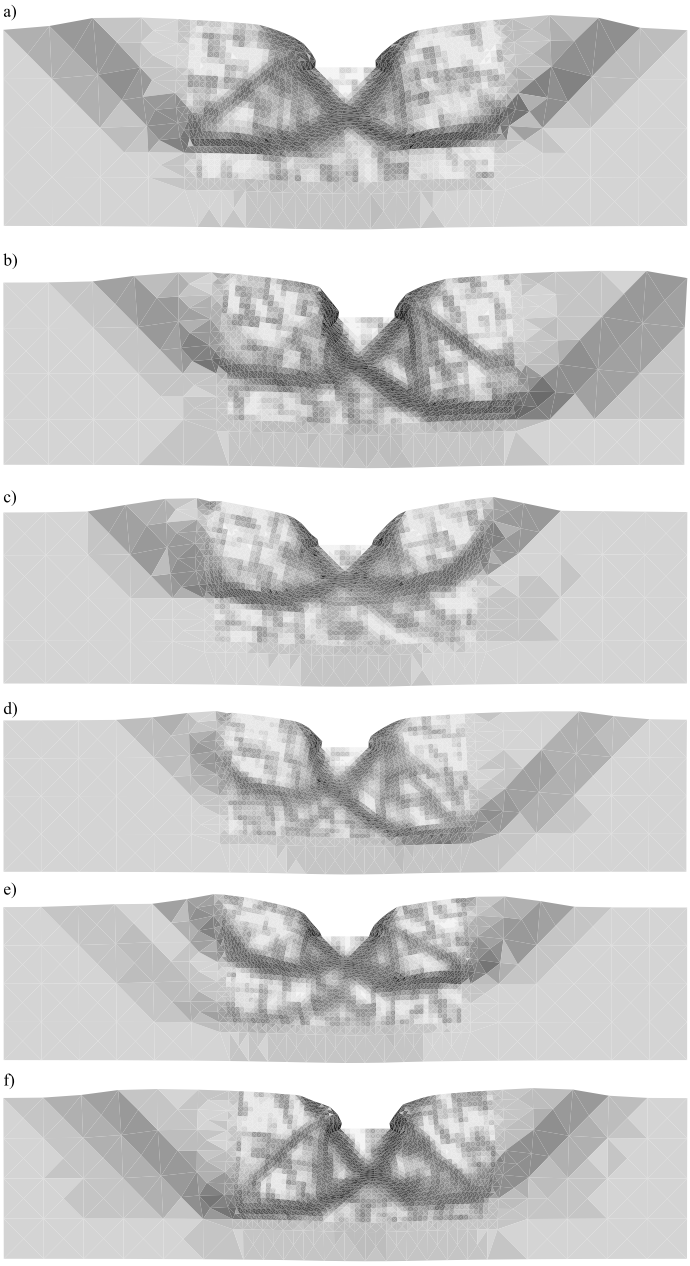

Fig. 11. Distributions of void ratio at residual state (s/B_o = 0.5–0.6) close to the footing from FE calculations with random distribution of e_o for six different cases (B_o = 2.5 cm)

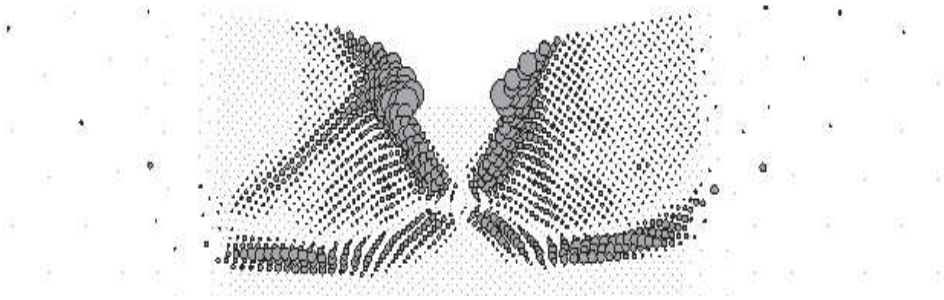

Fig. 12. Distributions of Cossearat rotation at residual state close to the footing from FE-calculations with random distribution of e_o for the case '2' of Fig. 8b (B_o = 2.5 cm)

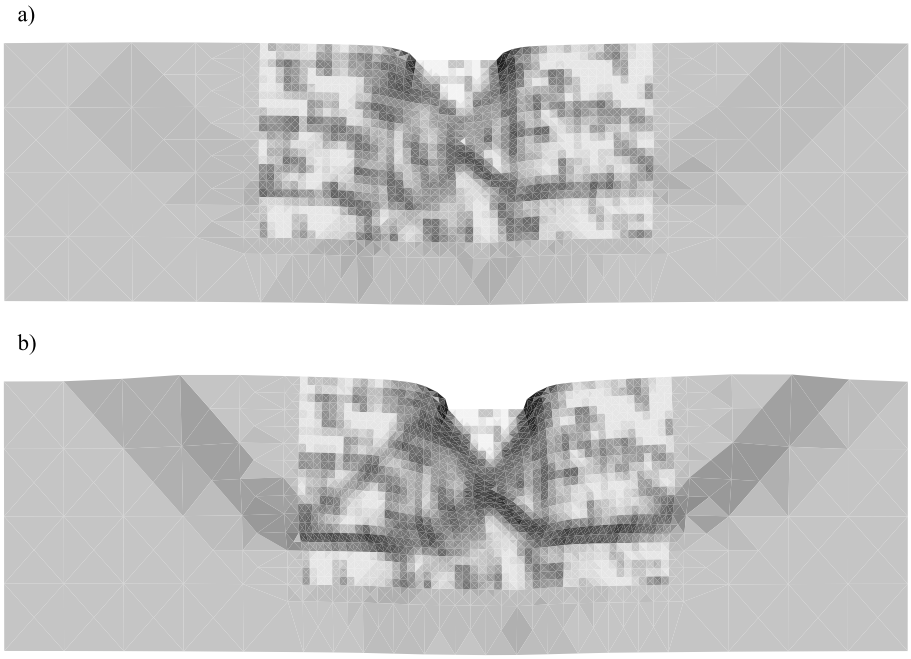

Fig. 13. Distributions of void ratio close to the footing from FE calculations with random distribution of e_o for the case '2' of Fig. 8b (B_o = 2.5 cm): a) s/B_o = 0.2, b) s/B_o = 0.3

The evolution of the normalized vertical force is shown in Fig. 14 when e_{d0} = 0.44 and B_o = 2.5 cm (in this case, the generated random field of e_o was not cut off below e_d). The distributions of e_o close to the footing for three different cases (cases No. '1', '2' and '7' of Fig. 6) are shown in Fig. 15 at the residual state for B_o = 2.5 cm.

In the case of the uniform initial void ratio, the maximum normalized vertical force $N_{\max}$ is with e_{d0} = 0.44 ($N_{\max}$ = 244) 40% smaller than in the case with e_{d0} = 0.51 ($N_{\max}$ = 360) and is in satisfactory agreement with laboratory tests ($N_{\max}$ =

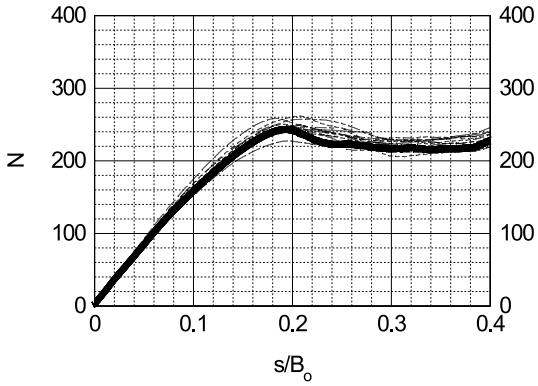

Fig. 14. Evolution of normalised vertical force $N = 2q/(\gamma_d B_o)$ versus normalised vertical displacement s/B_o from FE-calculations with uniform (thick solid line) and random distribution of e_o (dotted lines) with $B_o = 2.5$ cm and $e_{d0} = 0.44$ (q – average contact footing pressure, γ_d – initial unit weight, B_o – footing width)

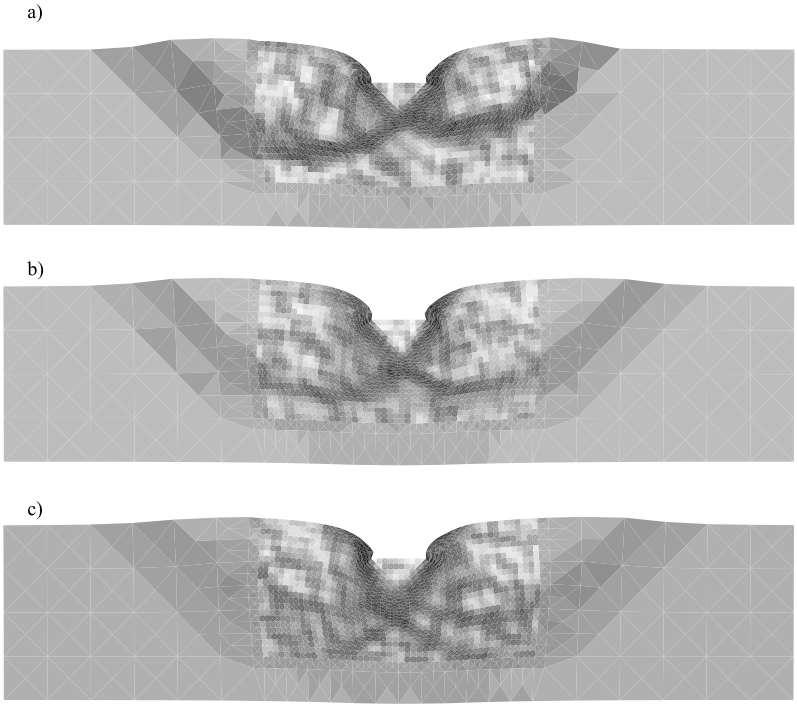

Fig. 15. Distributions of void ratio at residual state close to the footing from FE-calculations with random distribution of e_o for 3 different cases ($B_o = 2.5$ cm, $e_{d0} = 0.44$)

230) (Fig. 1). On the other hand, the rate of softening is too small. In the case of a random distribution of e_o, the mean normalized vertical force $N_{\max} = 248$ is again higher than the deterministic value ($N_{\max} = 244$) as in the case of a small size

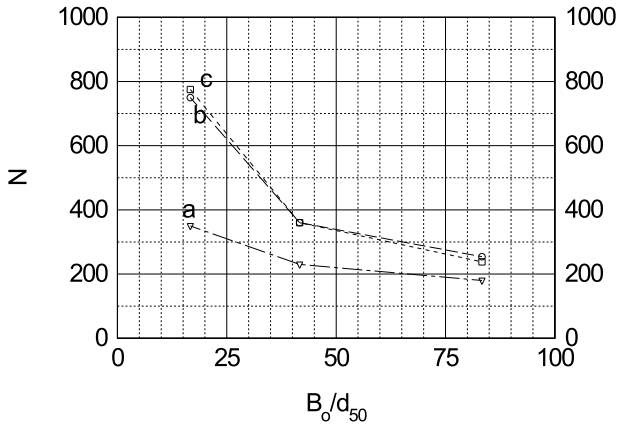

Fig. 16. Normalised vertical force $N = 2q/(\gamma_d B_o)$ versus ratio B_o/d_{50} from: a) experiments (Tatsuoka et al 1997), b) deterministic FE calculations with $e_{d0} = 0.51$, c) statistical FE calculations with $e_{d0} = 0.51$ (q – average contact footing pressure, γ_d – initial unit weight, B_o – footing width, d_{50} – mean grain diameter)

footing with $e_{d0} = 0.51$. The pattern of shear zones can be again non-symmetric as in the case with $e_{d0} = 0.51$ (the differences between two cases are negligible).

A summary of the calculated vertical normalized forces $N_{\max}$ ($e_{d0} = 0.51$) as compared to the experimental results by Tatsuoka et al (1997) is shown in Fig. 16.

6. Conclusions

The following conclusions can be drawn from our non-linear FE-investigations of deterministic and statistical size effects in plane strain footings on sand:

The well known deterministic size effect (decrease of the bearing capacity with increasing specimen size) is reproduced by FE modeling. It is caused by both shear localization and pressure level unless the initial void ratio is appropriately scaled.

The statistical size effect is significantly weaker than the deterministic one. The bearing capacity obtained from random sampling can be larger than a deterministic one in small-size and medium size model footings, in contrast to large-size model footings, which rather obey the weakest link model. The difference between a deterministic material strength and a mean statistical strength grows with increasing footing width. Such behaviour is also typical for quasi-brittle materials during uniaxial extension and bending.

The number, shape and placement of shear zones are all very sensitive to the distribution of initial void ratio.

The numerical calculations of size effects in granular bodies will be continued. More realistic, i.e. non-symmetric random fields of the distribution of the initial void ratio will be produced (Tejchman and Gorski 2009) on the basis of X-ray Computed Tomography with an assembly of spheres and real sand grains (Sheppard et al 2006,

Aste et al 2007). In addition, the FE analyses will be carried out with a stochastic distribution of initial stresses (Niemunis et al 2005) and grain diameter (Gorski et al 2008).

References

Aste T., Di Matteo T., Saadatfar M. and Senden T. J. (2007) An invariant distribution in static granular media, *Europhysics Letters* (in press).

Bazant Z. and Planas J. (1998) *Fracture and size effect in concrete and other quasi-brittle materials*, CRC Press LLC.

Bätcke W. (1982) Tragfähigkeit gedrungener Körper im geneigten Halbraum, *Dissertation at the University Braunschweig.*

Bauer E. (1996) Calibration of a comprehensive hypoplastic model for granular materials, *Soils and Foundations*, **36** (1), 13–26.

Bielewicz E. and Górski J. (2002) Shell with random geometric imperfections. Simulation-based approach, *International Journal of Non-linear Mechanics*, **37** (4–5), 777–784.

Ehlers W., Ramm E., Diebels S. and D'Addetta G. A. (2003) From particle ensembles to Cosserat continua: homogenisation of contact forces towards stresses and couple stresses, *Int. J. Solids Structures*, **40**, 6681–6702.

Fenton G. A. and Griffiths D. V. (2002) Probabilistic foundation settlement on spatially random soil, *J. Geotech. Geoenvironment. Eng.*, **128** (5), 381–389.

Górski J. (2006) *Non-linear models of structures with random geometric and material imperfections simulation-based approach*, Gdansk University of Technology, 68.

Górski J., Bobiński J. and Tejchman J. (2008) FE-simulations of size effects in granular and quasi-brittle materials, *Proc. Int. Conference Solmech*, Gdańsk, (eds.: Kotulski Z., Kowalczyk P. and Sosnowski W.), IPPT, 216–217.

Groen A. E. (1997) Three-dimensional elasto-plastic analysis of soils, *PhD Thesis*, Delft University, 1–114.

Gudehus G. (1996) Comprehensive constitutive equation for granular materials, *Soils and Foundations*, **36** (1), 1–12.

Gudehus G. and Nübel K. (2004) Evolution of shear bands in sand, *Geotechnique*, **113**, 54 (3), 187–201.

Gudehus G. (2006) Seismo-hypoplasticity with a granular temperature, *Granular Matter*, **8** (2), 93–102.

Herle I. and Gudehus G. (1999) Determination of parameters of a hypoplastic constitutive model from properties of grain assemblies, *Mechanics of Cohesive-Frictional Materials*, **4**, 5, 461–486.

Herle I. and Kolymbas D. (2004) Hypoplasticity for soils with low friction angles, *Computers and Geotechnics*, **31**, 365–373.

Huang W. X, Wu W, Sun D. A. and Sloan S. (2006) A simple hypoplastic model for normally consolidated clay, *Acta Geotech.*, **1** (1), 15–27.

Hurtado J. E. and Barbat A. H. (1998) Monte Carlo techniques in computational stochastic mechanics, *Archives of Computational Method in Engineering*, **5** (1), 3–30.

Jarzombek G. (1989) Experimentelle und numerische Untersuchungen zum Spannungs-Verformungsverhalten von trockenem Sand am Beispiel einer Streifengründung, *PhD thesis*, Universität Weimer, Germany.

Knabe W., Przewłócki J. and Różyński G. (1998) Spatial averages for linear elements for two-parameter random field, *Prob. Engng. Mech.*, **13** (3), 147–167.

Maier T. (2002) Numerische Modellierung der Entfestigung im Rahmen der Hypoplastizität, *PhD Thesis*, University of Dortmund.

Masin D. (2005) A hypoplastic constitutive model for clays, *Int. J. Numer. and Anal. Meths. in Geomech.*, **19** (4), 311–336.

Masin D. and Herle I. (2007) Improvement of a hypoplastic model to predict clay behaviour under undrained conditions, *Acta Geotech.* (in press).

Mühlhaus H.-B. (1990) Continuum models for layered and blocky rock. In: *Comprehensive Rock Engineering* (J. A. Hudson, Ch. Fairhurst, editors), Pergamon, 2, 209–231. **2 to No. czy Vol.?**

Niemunis A. and Herle I. (1997) Hypoplastic model for cohesionless soils with elastic strain range, *Mechanics of Cohesive-Frictional Materials*, **2** (4), 279–299.

Niemunis A. (2003) Extended hypoplastic models for soils, *Habilitation Monography*, Gdańsk University of Technology.

Niemunis A., Wichtmann T., Petryna Y. and Triantafyllidis T. (2005) Stochastic modeling of settlements due to cyclic loading for soil-structure interaction. In: *Proc. Int. Conf. Structural Damage and Lifetime Assessment*, Rome.

Nübel K. (2002) Experimental and numerical investigation of shear localisation in granular materials, *Publication Series of the Institute of Soil and Rock Mechanics*, University Karlsruhe, 62.

Nûbel K. and Huang W. X. (2004) A study of localized deformation pattern in granular media, *Computer Methods in Applied Mechanics and Engineering*, **193** (27–29), 2719–2743.

Oda M. (1993) Micro-fabric and couple stress in shear bands of granular materials. In: *Powders and Grains* (C. Thornton, editor), Rotterdam, Balkema, 161–167.

Pasternak E. and Mühlhaus H.-B. (2001) Cosserat continuum modelling of granulate materials. In: *Computational Mechanics – New Frontiers for New Millennium* (eds.: Valliappan S. and Khalili N.), Elsevier Science, 1189–1194.

Rondon H. A., Wichtmann T., Triantafyllidis T. and Lizcano A. (2007) Hypoplastic material constants for a well-graded granular material for base and subbase layers of flexible pavements, *Acta Geotechnica*, **2** (2), 113–126.

Schäfer H. (1962) *Versuch einer Elastizitätstheorie des zweidimensionalen ebenen Cosserat-Kontinuums. Miszellaneen der Angewandten Mechanik*, Festschrift Tolmien W., Berlin, Akademie-Verlag.

Sheppard A., Knackstedtr M., Senden T. and Saadatfar M. (2006) Analysis of granular materials using X-ray micro-CT, *Proc. 20th Canberra International Summer School and Workshop on Granular Material*, 53–53.

Steenfelt J. S. (1979) Scale effect on bearing capacity factor, *Report of the Danish Geotechnical Institute*, Copenhagen.

Tamagnini C., Viggiani C. and Chambon R. (2000) A review of two different approaches to hypoplasticity. In: *Constitutive Modeling of Granular Materials* (D. Kolymbas, ed.), Heidelberg, Springer, 107–145.

Tatsuoka F., Okahara M., Tanaka T., Tani K., Morimoto T. and Siddiquee M. S. A. (1991) Progressive failure and particle size effect in bearing capacity of footing on sand, *Proc. of the ASCE Geotechnical Engineering Congress*, **27** (2), 788–802.

Tatsuoka F., Goto S., Tanaka T., Tani K. and Kimura Y. (1997) Particle size effects on bearing capacity of footing on granular material. In: *Deformation and Progressive Failure in Geomechanics* (eds.: A. Asaoka, T. Adachi and F. Oka), Pergamon, 133–138.

Tejchman J. and Wu W. (1993) Numerical study on shear band patterning in a Cosserat continuum, *Acta Mechanica*, **99**, 61–74.

Tejchman J. and Bauer E. (1996) Numerical simulation of shear band formation with a polar hypoplastic model, *Computers and Geotechnics*, **19** (3), 221–244.

Tejchman J. and Herle I. (1999) A "class A" prediction of the bearing capacity of plane strain footings on granular material, *Soils and Foundations*, **39** (5), 47–60.

Tejchman J. and Gudehus G. (2001) Shearing of a narrow granular strip with polar quantities, *J. Num. and Anal. Methods in Geomechanics*, **25**, 1–18.

Tejchman J. (2004a) FE-simulations of a direct wall shear box test, *Soils and Foundations*, **44** (4), 67–81.

Tejchman J. (2004b) Influence of a characteristic length on shear zone formation in hypoplasticity with different enhancements, *Computers and Geotechnics*, **31** (8), 595–611.

Tejchman J. and Niemunis A. (2006) FE-studies on shear localization in an anisotropic micro-polar hypoplastic granular material, *Granular Matter*, **8** (3–4), 205–220.

Tejchman J., Bauer E. and Wu W. (2007) Effect of texturial anisotropy on shear localization in sand during plane strain compression, *Acta Mechanica*, **189** (1–4), 23–51.

Tejchman J. and Wu W. (2009) FE-investigations of non-coaxiality and stress-dilatancy rule in dilatant granular bodies within micro-polar hypoplasticity, *Int. Journal for Numerical and Analytical Methods in Geomechanics*, **33** (1), 117–142.

Tejchman J. and Górski J. (2008a) Deterministic and statistical size effect during shearing of granular layer within a micro-polar hypoplasticity, *Int. Journal for Numerical and Analytical Methods in Geomechanics*, **32** (1), 81–107.

Tejchman J. and Górski J. (2008b) Computations of size effects in granular bodies within micro-polar hypoplasticity during plane strain compression, *Int. J. for Solids and Structures*, **45** (6), 1546–1569.

Tejchman J. and Wu W. (2009) FE-investigations of shear localization in granular bodies under high shear rate, *Granular Matter*, doi:10.1007/s10035-009-0128-4.

Tejchman J. (2008) *FE modeling of shear localization in granular bodies with micro-polar hypoplasticity*, Springer (eds.: Borja R. and Wu W.).

Tejchman J. and Gorski J. (2009) Modeling of bearing capacity of footings on sand within stochastic micro-polar hypoplasticity, *Intern. Journal for Numerical and Analytical Methods in Geomechanics*, 2009 (submitted).

Walukiewicz H., Bielewicz E. and Górski J. (1997) Simulation of nonhomogeneous random fields for structural applications, *Computers and Structures*, **64** (1–4), 491–498.

Wang C. C. (1970) A new representation theorem for isotropic functions, *J. Rat. Mech. Anal*., **36**, 166–223.

Vanmarcke E.-H. (1983) *Random Fields: Analysis and Synthesis*, Cambridge, MIT Press.

Weibull W. (1951) A statistical theory of the strength of materials, *Journal of Applied Mechanics*, **18** (9), 293–297.

Weifner T. and Kolymbas D. (2008) Review of two hypoplastic equations for clay considering axisymmetric element deformations, *Comp. Geotech*., doi:10.1016/j.compgeo.2007.12.001.

Wernick E. (1978) Tragfähigkeit zylindrischer Anker in Sand unter besonderer Berücksichtigung des Dilatanzverhaltens, *Publication Series of the Institute for Rock and Soil Mechanics*, University Karlsruhe 75.

von Wolffersdorff P. A. (1996) A hypoplastic relation for granular materials with a predefined limit state surface, *Mechanics Cohesive-Frictional Materials*, **1** (3), 251–271.

Wu W. and Kolymbas D. (2000) Hypoplasticity then and now. In: *Constitutive Modeling of Granular Materials* (ed. Kolymbas D.), Heidelberg, Springer, 57–105.